



# High-performance supercapacitor based on self-heteroatom-doped porous carbon electrodes fabricated from *Mikania micrantha*

Mohammed Jalalah<sup>1,2</sup> · HyukSu Han<sup>3</sup> · Arpan Kumar Nayak<sup>4</sup> · Farid A. Harraz<sup>2,5</sup>

Received: 8 November 2023 / Revised: 3 January 2024 / Accepted: 8 January 2024 / Published online: 27 January 2024  
© The Author(s), under exclusive licence to Springer Nature Switzerland AG 2024

## Abstract

Applications, economic advantage, and effective waste management have sparked much interest in porous carbon compounds synthesized from renewable and biowaste resources. Self-heteroatom-doped carbon compounds have recently been made using various biological precursors. This study investigates the ease of preparing biomass-derived porous carbon (BPC) matrices from raw and verdant *Mikania micrantha* leaves using a direct activation and pyrolysis procedure. With the aid of preactivation and pyrolysis, BPC materials can be synthesized with a high surface area of  $850.62 \text{ m}^2 \text{ g}^{-1}$  and total pore volume of  $0.85 \text{ cm}^3 \text{ g}^{-1}$ . Raman spectra reveal the successful creation of pores and enhanced structural disorder following carbonization account by achieving higher intensity ratio of the D band to the G band (ID/IG) of 0.97. At a current density of 1 A/g, the BPC materials MM-700 exhibit a specific capacitance of 393 F/g. Interestingly, the MM-700 BPC materials have a greater capacitive contribution to charge accumulation during the electrochemical reactions. The BPC material MM-700 solid-state device manufactured with a PVA-H<sub>2</sub>SO<sub>4</sub> gel electrolyte has a specific capacitance of 119 F/g at 1 A/g current density and a power density of 13.284 kW/kg at 30 A/g current density. Even at a high current density of 30 A/g, the synthesized porous carbon materials retain a high specific capacitance. Moreover, the MM-700 BPC material exhibits outstanding stability in both three- and two-electrode systems in strong acidic electrolyte.

**Keywords** *Mikania micrantha* leaves · Hetero-atom dope · Pyrolysis · Supercapacitor · Sol-state device

---

Mohammed Jalalah and HyukSu Han have equal contribution.

- ✉ Mohammed Jalalah  
jalalah@gmail.com
- ✉ Arpan Kumar Nayak  
aknayakju@gmail.com
- ✉ Farid A. Harraz  
faharraz@nu.edu.sa

- <sup>1</sup> Department of Electrical Engineering, College of Engineering, Najran University, Najran 11001, Saudi Arabia
- <sup>2</sup> Promising Centre for Sensors and Electronic Devices (PCSED), Advanced Materials and Nano-Research Centre, Najran University, P.O. Box: 1988, Najran 11001, Saudi Arabia
- <sup>3</sup> Department of Energy Science, Sungkyunkwan University, 2066 Seobu-Ro, Suwon 16419, Republic of Korea
- <sup>4</sup> Regional Institute of Education, National Council of Educational Research and Training (NCERT), Mysore 570006, India
- <sup>5</sup> Department of Chemistry, Faculty of Science and Arts at Sharurah, Najran University, Sharurah 68342, Saudi Arabia

## 1 Introduction

The imminent depletion of fossil fuels and rising worries about environmental contamination necessitate the development of novel energy storage methods. Equipment for storing and transforming energy is a topic of intense scientific interest [1, 2]. Superior cyclability and remarkable power density are only two of the reasons why supercapacitors are an exciting new category of energy storage devices. Due to their high power density, quick charge/discharge characteristics, and outstanding cycle durability, the electrochemical double-layer capacitors (EDLC) are considered one of the most promising energy storage devices [3]. However, the commercially available energy density of EDLC is currently less than  $10 \text{ Wh kg}^{-1}$ , which severely restricts the technology's potential [4]. One of the most crucial aspects of supercapacitors is the electrode materials that significantly affect their electrochemical performances. Therefore, it is necessary to design materials conducive to charge storage as the electrode materials of EDLC to obtain enhanced electrochemical storage. It is well documented that macro/

meso/microporous carbon nanomaterials are among the most promising electrode materials for energy storage devices. Micropores, in particular, can increase the surface area available to ions, increasing capacitance and energy density [5]. Macropores act as ion buffer reservoirs, decreasing the diffusion barrier to the inner pore structure, while mesopores may supply the locations for charge storage and enhance ion transport [6, 7]. Therefore, among many other options, such as zeolites and porous silica, porous materials are among the best candidates for electrode materials in EDLC [8].

Researchers are constantly trying to find better ways to synthesize hierarchically porous carbon materials to achieve a well-developed pore structure with customized porosity. Supercapacitors and lithium batteries, for example, rely heavily on porous carbon. Since these materials are indispensable, and these devices are expected to increase steadily over the next few years, there will be a high demand for porous carbons. Therefore, maximizing the production of carbon materials for these uses is essential. Both scalability and environmental friendliness are required to produce porous carbons without the help of any corrosive and harmful substances [9]. When it comes to EDLC, good storage performance can be achieved by using advanced electrode materials. Carbon-based materials are the most well known and widely used right now because they have a high specific surface area and stable physicochemical characteristics [10]. Researchers have talked about how to use activated carbon, carbon nanotubes (CNTs), graphene, and templated carbon in EDLC [11]. Activated carbon is widely utilized in commercial supercapacitors because of its inexpensive cost and high specific surface area [12]. However, its poor rate performance is attributed to inefficient power management and tortuous micropores that impede electron and ion transit. Furthermore, carbon nanotubes (CNTs) and graphene have been investigated as electrodes for EDLC to enhance power handling [13–17]. However, their use in practical supercapacitors is still hampered by issues such as CNTs' low specific surface area and the reduction process's restacking of graphene layers, which makes the graphene structure dense without preserving the effective surface area for electrolyte accessibility [18–25]. For this reason, the hunt for a unique carbon with high electric conductivity and the ideal pore size is highly desirable.

The carbon precursors that produce porous carbons should be easily accessible, inexpensive, and renewable materials such as biomass or biomass-based products. Typically, templates or carriers are used to create a hierarchically porous structure in carbon materials, and then in situ, doping or post-treatment in a specific chemical environment is used to integrate heteroatoms [26, 27]. Large-scale production and practical applications are severely constrained by issues such as the complexity of the synthesis procedure, the high cost of templates and precursors, and the inability to

modify the porosity structure. The electrochemical capacitance performance of biomass-based carbons is on par with or even superior to that of commercial activated carbons. Large-scale manufacturing of several of them as commercial activated carbons is challenging from the perspectives of cost-effectiveness, earth availability of precursors, and simple synthesis. As a result, there is an urgent need for more readily available, renewable, inexpensive, and high-quality biomass or its derivatives to meet the demand for carbons in numerous industries, particularly supercapacitors.

This research investigates how easily biomass-derived porous carbon (BPC) matrices can be prepared from raw and green *Mikania micrantha* leaves via a direct activation and pyrolysis procedure. The biomass of leaves was converted into a nanoflake-like porous carbon by a cost-effective procedure. Synthesized BPC materials show large surface area and pore volume with the help of the preactivation and carbonization pathway. When the BPC elements MM-700 are put together, they have a specific capacitance of 393 F/g at a current density of 1 A/g. Interestingly, the BPC materials MM-700 could provide a more prominent capacitive contribution to accumulate the overall charge during the electrochemical reaction. The manufactured solid-state device of BPC materials MM-700 using a PVA-H<sub>2</sub>SO<sub>4</sub> gel electrolyte have a specific capacitance of 119 F/g at 1 A/g current density along with a maximum energy density of 55.55 Wh/kg and power density of 13.284 kW/kg at 30 A/g current density. Prepared permeable carbon materials exhibited excellent specific capacitance retention even at high current density of 30 A/g. Moreover, BPC materials MM-700 displayed excellent stability in both three and two-electrode system in strong acidic electrolyte.

## 2 Experimental

The chemicals (Section 1.1), the preparation of BPC materials (Section 1.2), and the instrumentation (Section 1.3) are explained in detail in the Supporting Information.

### 2.1 Electrochemical measurement and electrode fabrication

The typical three-electrode system (graphite sheet, Ag/AgCl, and Pt wire as working, reference, and counter electrode), as well as a two-electrode system, was used to conduct cyclic voltammetric (CV) and galvanostatic charge-discharge (GCD) studies. The BPC components (1 mg), binder polyvinylidene difluoride (PVDF), and solvent N-methyl-2-pyrrolidone (NMP) were mixed in a mortar and mashed into a slurry. The working electrode was prepared by spreading the premade paste on a sheet of graphite (1 × 1 cm) and drying it in a vacuum oven for one night

before using it in an electrochemical application. The thickness of the prepared electrode is 0.5 mm. To determine the optimal electrolyte for an electrochemical application, we tested 0.5 M H<sub>2</sub>SO<sub>4</sub>, 0.5 M Na<sub>2</sub>SO<sub>4</sub>, and 1 M KOH. The capacitance measurement input to the graphite sheet in an acidic electrolyte is nearly negative (Fig. S1, Supporting Information). The generated BPC materials' electrochemical impedance spectra (EIS) were examined at a bias potential of 0.059 V (vs. RHE) and an amplitude of 5 mV spanning the frequency range of 0.1 Hz to 100 kHz. The specific capacitance was calculated by plugging the respective CV diagrams of the two electrode systems into the following Eq. (1) [28, 29]:

$$C_{sp} = \frac{\int_{V_1}^{V_2} idv}{m\vartheta(V_2 - V_1)} \quad (1)$$

Each option explains its function. Specific capacitance, abbreviated as “ $C_{sp}$ ,” is measured in Farads per gram. In this equation, “ $m$ ” represents the total mass of the electrode materials, and “ $\int_{V_1}^{V_2} idv$ ” indicates the total charge. Scanning rates are denoted by “ $\vartheta$ ” and the potential window is written as  $(V_2 - V_1)$ . Similar to how the following Eq. (2) was used to derive the galvanostatic CD-specific capacitances:

$$C_{sp} = \frac{it}{m\Delta V} \quad (2)$$

while “ $C_{sp}$ ” represents the specific capacitance (F/g), “ $i$ ” represents the constant discharge current, “ $t$ ” represents the discharge time, “ $m$ ” represents the active electrode mass materials, and “ $V$ ” represents the potential window. To calculate energy density (ED, Wh/kg) and power density (PD, kW/kg), the following formulae were used (Eqs. 3 and 4).

$$ED = \frac{C_{sp} V^2 \times 1000}{2 \times 3600} \quad (3)$$

$$PD = \frac{ED \times 3600}{t \times 1000} \quad (4)$$

Discharge time is denoted by  $t$ . The electrochemical analysis was performed using a CHI instrument electrochemical workstation.

## 2.2 PVA-H<sub>2</sub>SO<sub>4</sub> gel electrolyte fabrication

An electrolyte gel composed of polyvinyl alcohol and sulfuric acid (PVA-H<sub>2</sub>SO<sub>4</sub>) was manufactured via the following steps: In a beaker, we mixed 10 ml of distilled water, 1 g of PVA, and 1 ml of concentrated H<sub>2</sub>SO<sub>4</sub>. The suspension solution was heated to 80 °C and stirred constantly to create a thick liquid. After the gel cooled to room temperature, it appeared translucent.

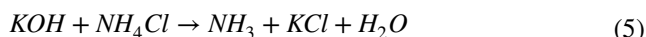
## 2.3 Synchronous construction of a symmetric solid-state supercapacitor

The PVA-H<sub>2</sub>SO<sub>4</sub> gel electrolyte used in the symmetric solid-state supercapacitor device of the activated HAPC materials was chosen because it allows for a clearer understanding of the true capacitive behavior of the developed materials based on porous carbon. Using the aforementioned technique, the functioning electrodes are made ready. The PVA-H<sub>2</sub>SO<sub>4</sub> gel electrolyte was then applied to the materials based on the porous carbon electrode's active area. The SSSD was built by squeezing two functional electrodes together to create a sandwich. The gel electrolyte was left out overnight at room temperature to harden. The galvanostatic charge/discharge tests' working potential range and cyclic voltammograms (CV) were set at 1.8 V.

## 3 Results and discussion

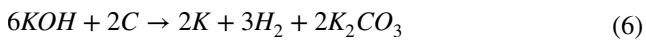
### 3.1 Preparation of materials based on porous carbon from *Mikania micrantha*

*Mikania micrantha* has corrugated stems that can reach a maximum height of 6 m (20 ft) and leaves that are 4–13 cm (1.6–5.1 in) long with a heart-shaped base and a pointed tip. A total of 4.5–6.0-mm (0.18–0.24 in) clumps of white blossoms are present. In traditional medicine systems, *Mikania micrantha* leaves are employed as ulcer preventatives and wound healers. Additionally, the leaves are used as an antimicrobial, antipyretic, and anti-inflammatory agent, as well as an anti-cold congestion decoction [30]. The raw, green leaves of *M. micrantha* contain various chemical components. It can be used for a variety of medical purposes. This plant's anticancer, antioxidant, anti-diabetic, antibacterial, and anti-diarrheal characteristics are just the tip of the iceberg of its therapeutic potential. These functions can be attributed to the presence of phytochemicals such as flavonoids, alkaloids, saponins, tannins, phenol, and carbohydrates [30]. Pectin, crude fiber, carotenoids, water, oil, and polyphenols are only some of the nutrients found in the raw green leaves. Carbohydrates are the primary building blocks of the synthesis, or carbon precursors.



With the help of the KOH activator, there was first a solid-solid reaction, and then a solid-liquid one. The KOH also decreased throughout the process, becoming K metal. Carbon precursors undergo oxidation, yielding carbon dioxide (CO<sub>2</sub>) and carbonate (CO<sub>3</sub>). The cross-reaction occurs at the same time. K<sub>2</sub>CO<sub>3</sub> is produced at temperatures between 400 and 600 °C during the activation phase. When heated

over 600 °C,  $K_2CO_3$  dissociates into  $K_2O$  and  $CO_2$ . Over 800 °C will be reached at the end of the process. Carbon precursors undergo chemical reactions with the produced  $CO/CO_2$  and K compounds at temperatures exceeding 700 °C. This chemical activation process is permanent because it causes the carbon lattice structure to expand. The resulting carbon materials have an exceptionally high level of microporosity. The fundamental mechanism is depicted by the following Eqs. (6)–(10) [31].



The heteroatom content, surface area, and porosity of the resultant carbon may all be linked back to the reaction temperature and KOH. Using a carbon precursor and potassium hydroxide (KOH) ratio of 1:1, BPC materials were synthesized at varying pyrolysis temperatures.

### 3.2 Morphological and structural analysis

Scanning electron microscopic (SEM) and transmission electron microscopic (TEM) measurements were used to analyze the microstructures and morphologies of the as-prepared samples. Images of the prepared biomass-derived porous carbon (BPC) sample taken with the scanning electron microscope are shown in Fig. 1a–f.

When BPC is carbonized, its porous framework becomes highly developed and is inhabited with nanoflakes. Both the highly developed nutrition and metabolic channels of the leaves derived from *M. micrantha* biomass materials and the pore channels created by moisture and small-molecule gases released after a thermal breakdown in the presence of a KOH activator were credited with contributing to the nanoflakes architectures of the BPC materials [32]. Because of these passages, the KOH activator can reach deep into the carbon materials, interacting with them to increase the pore diameters. The BPC-MM-600 shows fewer holes and nanoparticles at lower temperatures (Fig. 1a). Figure 1b demonstrates that the nanoflakes' uniformity increases, and their porosity structure becomes more systematic with increasing temperature. When heated above 800 °C, the product's internal structure begins to degrade, and the channel's inner walls become flimsy. We can see fewer nanoflakes (Fig. 1c). The roughening of the BPC materials' surface is proof that

the KOH activator reacts well with the carbon particles in the biowaste. The number of holes significantly rises after the addition of the KOH activator. This was because the biowaste included carbon matrices, which caused the pores to dilate and enlarge. According to EDX analysis, heteroatoms are present in the BPC framework MM-800 (Fig. S2b). The EDX analysis confirms the presence of heteroatoms in the synthesized BPC materials from the natural source. The microstructural features of the ready-made BPC framework MM-800 were better understood through transmission electron microscopy investigation. TEM measurement (Fig. 1g, h), which supplements the findings of FE-SEM, revealed the produced BPC framework MM-800 to have an interconnected nanoflake structure. Porosity in the carbon components of the constructed BPC framework MM-800 is clearly visible in TEM images, as illustrated in Fig. 1g. XRD and Raman spectroscopy were used to determine the degree of graphitization in the samples. On the other hand, Fig. S3 shows that the XRD patterns of BPC materials exhibit two diffraction peaks at  $2\theta$  values of 26.3 and 44.2, which are assigned to typical (002) and (101) reflections of graphitic carbon (JCPDS no. 41-1487); a broad peak was observed in BPC, indicating the amorphous carbon structure of *Mikania micrantha* leaves prior to graphitization (Fig. S3). The XRD data thus demonstrated the good crystallinity of the BPC sample synthesized in a single step. Raman spectroscopy (Fig. 1i) also provided evidence of the graphitic structure. Graphite's D band at  $1350\text{ cm}^{-1}$  is usually interpreted as representing defect sites or disordered  $sp^2$ -hybridized carbon atoms, the G band at  $1580\text{ cm}^{-1}$  as representing the in-plane vibration of  $sp^2$ -bonded carbon atoms, and the 2D band at  $2800\text{ cm}^{-1}$  as representing the two phonon lattice vibration [33, 34]. Determining the degree of crystallization or defect density in carbon materials typically involves calculating the intensity ratio of the D band to the G band (ID/IG). BPC materials, MM-600, MM-700, and MM-800 all had ID/IG ratios of 0.93, 0.97, and 0.95, respectively. Creation of pores and enhanced structural disorder following carbonization account for the higher ID/IG values seen in BPC samples [33, 35, 36]. Raman spectra of MM-700, in comparison to other samples, revealed shorter D and G bands and a strong 2D band, both of which are indicative of a successful transformation of biomass into graphitic carbon [33, 36].

The pyrolysis temperature highly modulates the appearance and structure of the synthesized materials. Two crucial characteristics from an electrochemical viewpoint are the electrode conductivity and the electrode surface area [31, 37–42]. The contact area between the electrode and the electrolyte can be increased, and the conductivity can be increased if the specific surface area of the electrode is made more prominent [31, 37–42]. Good conductivity requires a pyrolysis stage at high temperatures, which has the added benefit of forming a hierarchical porous structure,

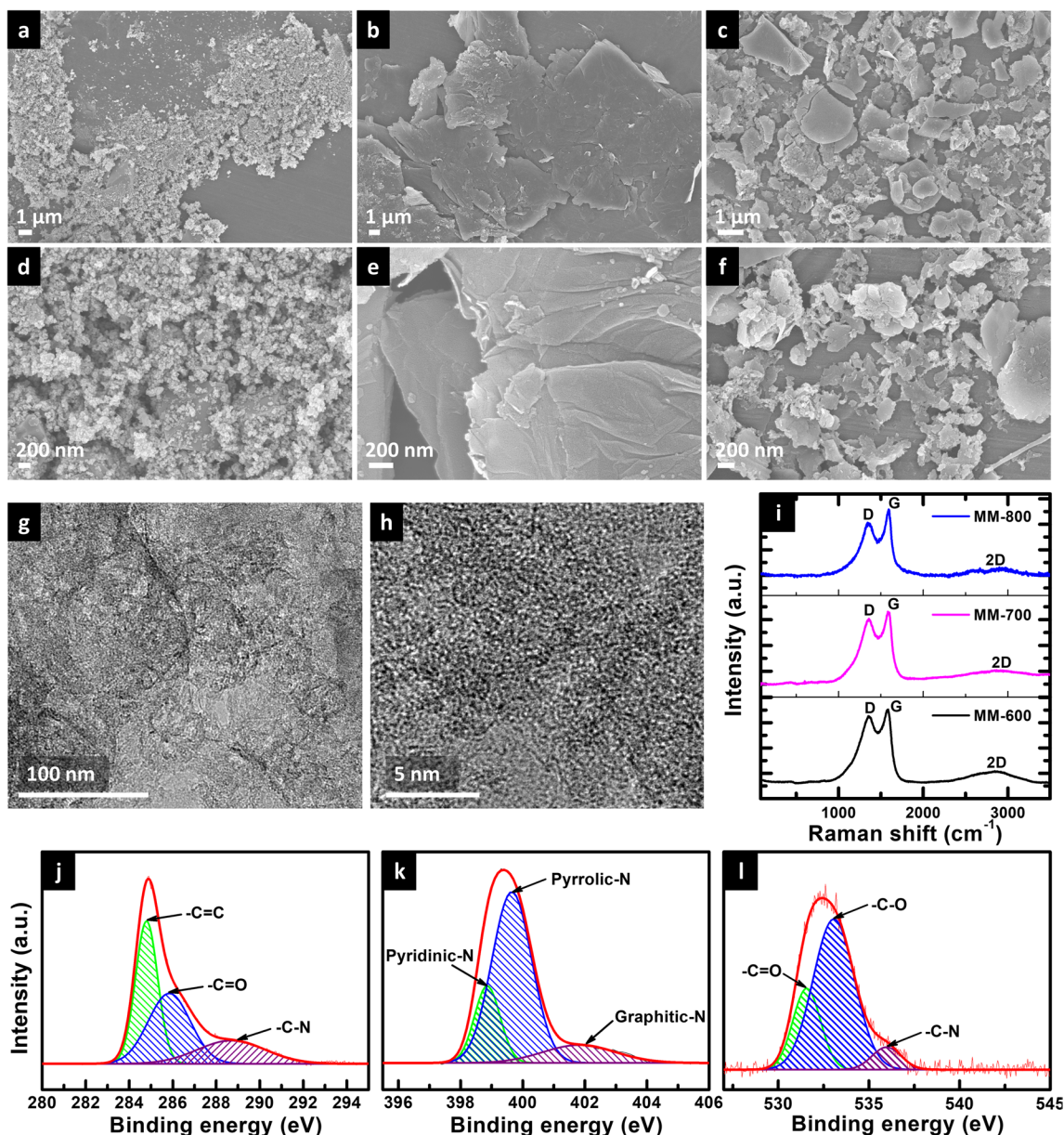


**Fig. 1** SEM images of biomass-derived porous carbon (BPC) from *Mikania micrantha* leaves using different pyrolysis temperatures and magnification. **a, d** BPC-MM-600, **b, e** BPC-MM-700, and **c, f** BPC-MM-800. **g** TEM and **h** HRTEM image

of the prepared BPC-MM-700. **i** Raman spectroscopy of BPC materials at changed initiation temperatures. High-resolution XPS spectrum of synthesized BPC MM-700 for (j) carbon, (k) nitrogen, and (l) oxygen

an indicator of a high specific surface area [31, 37–42]. At 77 K, the porosity was determined using nitrogen adsorption-desorption as shown in Fig. S4. All of them fit the profile of a type IV isotherm typical of mesoporous materials with an H4 hysteresis loop. It was clear that the porous textures varied depending on various samples. Micropores were evidenced by the existence of a strong adsorption inflection at low relative pressures and well-developed plateaus in the BPC sample's adsorption-desorption isotherm (Fig. S4), and the sample possessed a narrow pore size distribution. The

MM-700 sample had a high BET surface area, measuring 850.62 m<sup>2</sup> g<sup>-1</sup>, and a total pore volume of 0.85 cm<sup>3</sup> g<sup>-1</sup>, of which 0.75 cm<sup>3</sup> g<sup>-1</sup> was attributed to micropores. Electrolyte penetration and ion adsorption are aided by MM-800's wide accessible surface area and optimal pore size distribution, most of which come from micropores, leading to improved energy storage capacity. In contrast, the other BPC materials, MM-600 and MM-800, showed a lower BET surface area of 365 and 560.25 m<sup>2</sup> g<sup>-1</sup> and a very small total pore volume of 0.45 and 0.62 cm<sup>3</sup> g<sup>-1</sup> due to extensive corrosion and

degradation of the original structure using lower and higher pyrolyzed temperatures. XPS analysis provided additional confirmation of the elemental composition of the MM-700 sample (Fig. 1j–l). Survey spectra (Fig. S5) demonstrate that both materials include oxygen, nitrogen, and carbon, which are represented by three prominent peaks at binding energies of 532.6, 400.2, and 284.6 eV, respectively.

Figure 1(j–l) displays the deconvoluted XPS spectra for carbon, nitrogen, and oxygen. The C=C bond in the samples is responsible for the peak in the C1s spectra at the binding energy of 284.8 eV; C=O and C-N are produced at the binding energy of 285.65 eV and 288.63 eV, respectively [33, 35, 36, 43, 44]. Nitrogen is present in the resulting BPC framework MM-700. However, its presence may be broken down into its constituent pyridinic-N (398.3 eV), pyrrolic-N (400.1 eV), and graphitic-N (402.3 eV) atoms, as seen in Fig. 1k [33, 35, 36, 43, 44]. Incorporating heteroatoms into active carbon material matrices may improve the BPC framework's electrochemical characteristics. Doping heteroatoms into electrode materials is a primary way to boost their pseudo-capacitive property. The contribution of pseudocapacitance from BPC materials, which can take part in the faradic redox process, is bolstered by the presence of pyrrolic-N. Similarly, pyridinic-N-containing electrode materials enhance the wettability behavior of the electrode material [33, 35, 36, 43, 44]. Incorporating the heteroatom into the BPC matrix allows for the enhanced electrochemical performance of an MM-700-based electrode. Deconvolution of the O1s spectrum reveals three peaks, one each for C=O (531.5 eV), C-O (532.9 eV), and C-N (535.6 eV) (Fig. 1l) [33, 36]. In addition, the data show that the chemical composition of the three samples is comparable. The presence of oxygen on the surface of a material can contribute as a major impact on its electrochemical behavior, and this is true even for carbons that have been purposefully doped with other heteroatoms [45]. They can serve as redox-active functionalities and increase the wettability of carbon surfaces in aqueous solutions. Redox-active organic functional groups contribute a finite amount of faradaic charge to the overall specific capacitance. Increasing the amount of O can significantly increase the cell's volumetric and gravimetric capacitance and so serve as a crucial factor for boosting the overall performance of supercapacitors, albeit this typically works at the modest expense of the cell's power density.

### 3.3 Electrochemical analysis

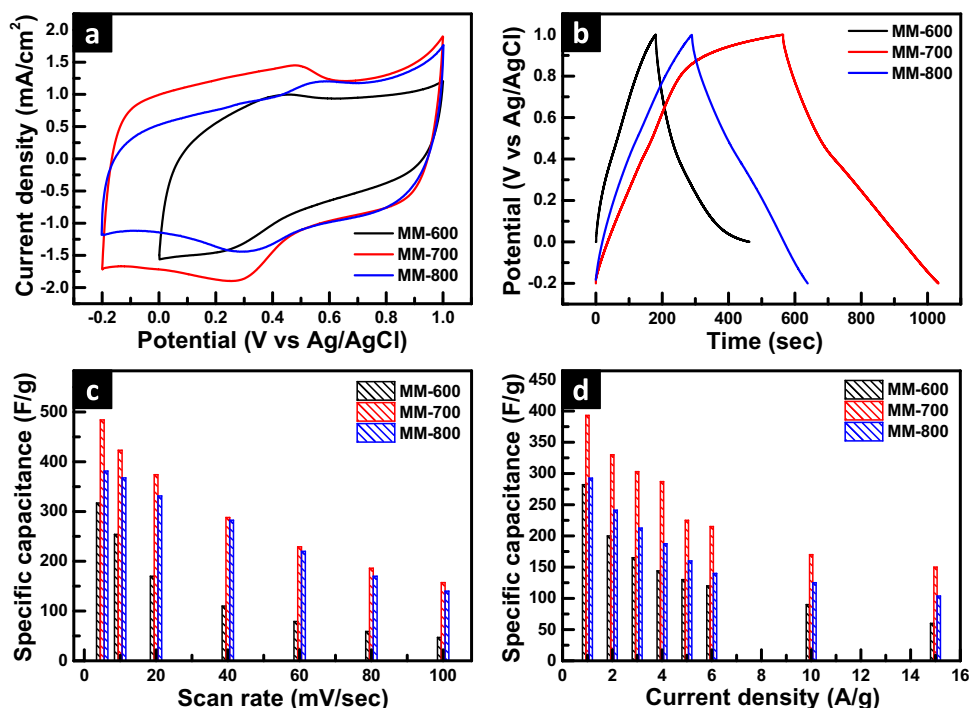
#### 3.3.1 Three-electrode application

Charge storage capabilities of biomass-derived porous carbon (BPC) samples were studied using cyclic voltammetry (CV), galvanostatic charge-discharge (GCD), and impedance analysis. In a three-electrode configuration, the potential

range is set between  $-0.2$  and  $1$  V relative to the Ag/AgCl reference electrode. Neutral ( $\text{Na}_2\text{SO}_4$ ), acidic ( $0.5$  M  $\text{H}_2\text{SO}_4$ ), and alkaline ( $1$  M KOH) electrolytes were all used in the system to distinguish the suitable supporting electrolyte. With a wide potential window of  $-0.2$  to  $1$  V vs. Ag/AgCl reference electrode at  $5$  mV/s scan rate (Fig. S6), the MM-700 materials exhibit specific capacitance ( $C_{\text{sp}}$ ) values of  $102$ ,  $484$ , and  $72$  F/g in the aforementioned electrolytes, respectively. The MM-700 uses  $\text{H}_2\text{SO}_4$  as its electrolyte and has a greater  $C_{\text{sp}}$  at a lower scan rate than other BPC architectures made with different annealing temperatures due to the smaller size of  $\text{H}^+$  ions in the supporting electrolyte. For this reason, all the electrochemical investigated is conducted in an acidic electrolyte [33, 35, 36].

The  $C_{\text{sp}}$  of the BPC materials MM-600, MM-700, and MM-800 in acidic electrolytes is  $317$ ,  $484$ , and  $381$  F/g, respectively, at a low scan rate of  $5$  mV/s (Fig. 2a). Because of its huge porous structure, active surface area, and the presence of heteroatoms in its interconnected carbon framework, the MM-700 may have the highest capacitance among synthetic carbon materials. In addition, the XRD, Raman, SEM, and BET investigations indicated that the pre-activated carbon precursor carbonization should occur at a temperature of  $700$  °C. But the synthesized BPC materials MM-600 show the lower working potential window in a three-electrode system, i.e.,  $0$  to  $+1$  V with a reference to Ag/AgCl electrode. This may be due to the poor graphitization, active surface area, and pore volume of the synthesized BPC materials. Moreover, the graphitization does not occur sufficiently at this temperature, as shown by XRD, Raman, and SEM. Redox-active N, O-containing functional groups in the materials are hypothesized to contribute to double-layer capacitance and pseudocapacitance by the distorted quasi-rectangular form of both curves with a hump in the potential barrier of  $-0.2$  V to  $1$  V in an acidic electrolyte. Increases in pseudocapacitance and specific capacitance can be inferred from MM-700's more pronounced hump and bigger ringed region. Figs. S7a, S8a, and S9a show the CV curves plotted against scan rate ( $10$  to  $100$  mV/s) for the synthesized BPC materials MM-600, MM-700, MM-800, respectively, using acidic electrolytes. The CV curve maintains its near-rectangular shape even as at increased scan rate, demonstrating the superior rate capability of BPC materials MM-700. However, a distinct phenomenon for BPC-based electrodes is seen as the scan rate increased from  $10$  to  $100$  mV/s. The quasi-rectangular shape gradually evolves into an irregular shape. In addition, studies have demonstrated that an increase in scan rate correlates with a drop in the  $C_{\text{sp}}$  of electrode materials. At low scan rates, the maximum amount of the inner region of the active electrode was used to carry out the electrochemical reaction. The greatest  $C_{\text{sp}}$  ever recorded is the result of scanning at the slowest possible speeds. This is because the highest  $C_{\text{sp}}$  is achieved at the slowest period,

**Fig. 2** **a** CV curves at a scan rate of 5 mV/s, **b** CD curves at a current density of 1 A/g, **c** a comparative diagram of specific capacitance with respect to the various scan rates, and **d** a comparative diagram of specific capacitance with respect to the various current densities of the synthesized BPC materials



allowing the inner charges to expand and permeate deeply into the hierarchical porous carbon matrices of the active electrode materials. Since the inner active section of electrochemically active materials often does not participate in electrochemical reactions, increasing the scan rate causes the  $C_{sp}$  of electrochemically active materials to decrease [43, 44, 46]. The manufactured BPC materials share the aforementioned electrochemical properties. All of the ready-made BPC materials exhibit reduced  $C_{sp}$  at increased scan rates. At a high scan rate of 100 mV/sec, the synthesized BPC materials MM-600, MM-700, and MM-800 provided respectively the specific capacitance of 47, 157, and 140 F/g under identical conditions using a three-electrode system (Figs. S7a, S8a, and S9a). At all scan rates, the synthesized BPC materials MM-700 demonstrate higher specific capacitance than other synthesized BPC materials MM-600 and MM-800 due to the higher surface area, pore volume, and optimum amount of doping of heteroatoms N and O in the carbon matrices (Fig. 2c).

The GCD curves of BPC-based electrodes were examined in a three-electrode system to examine the impact of chemical activators on the electrochemical behavior of the as manufactured BPC electrode materials. Different activation temperatures result in distinct constant current charge and discharge curves for activated carbon electrode materials, as shown in Fig. 2b. The diagrams show that the activated carbon electrodes behave like a conventional electric double-layer capacitor with an isosceles triangle configuration. The GCD curves are symmetrical, indicating that the electrodes are reversible [47]. The quasitriangular geometries of both profiles are indicative of

high Coulomb efficiency and reliable EDLC operation. The redox-active N, O functional groups cause pseudocapacitance, which accounts for the minor departure from triangular forms [48]. The capacitance is improved by the BPC's material's greater adsorption/desorption capacity for electrolyte ions, as indicated by the substantially longer discharge time of BPC MM-700 compared to other synthesized BPC MM-600 and MM-800. This squares nicely with the wider CV-encircled region of MM-800 that was previously discussed. The discharge profiles allowed us to determine that at current density of 1 A/g, the specific capacitance of MM-700 was 393 F/g. In contrast, other synthesized BPC-based materials MM-600 and MM-800 demonstrate the specific capacitance of 282 and 292 F/g under identical conditions (Fig. 2b). It is well known that carbon materials' surface area, pores, and channels are key properties since they allow for the formation of several electrical layers during the charging-discharging process. High Coulombic efficiency and electrochemical reversibility were indicated by the triangular and almost linear charge-discharge patterns found for the synthesized BPC materials with a minor IR drop. For nitrogen/sulfur-doped porous carbon sheets in an acidic electrolyte, Y Chen et al. reported a maximum specific capacitance of 132 F/g at an applied current density of 1 A/g [49]. Gao et al. reported that the synthesized porous carbon materials show a specific capacitance of 220 F/g which is synthesized from a crab shell as a carbon precursor [50]. The BPC electrode's GCD curves for a range of 2 to 15 A/g current densities are depicted in Figs. S7b, S8b, and S9b. Even as the current density increased from 1 to 15 A/g, the GCD curve maintains its ideal quasi-triangular shape, indicating that

the electrochemical properties are preserved. The synthesized BPC materials MM-700 show 215, 170, and 150 F/g at 6, 10, and 15 A/g current density using a three-electrode system under a wide potential window  $-0.2$  to  $1$  V vs. Ag/AgCl reference electrode. In contrast, other synthesized BPC materials, MM-600 and MM-800, demonstrate the specific capacitance of 120, 90, and 60 and 140, 125, and 103 F/g under identical current densities but different working potential windows. As mentioned above, the BPC MM-600 works under  $0$  to  $+1$  V vs. Ag/AgCl reference electrode in a three-electrode system. At all current densities, the synthesized BPC MM-700 shows a higher specific capacitance in a three-electrode system using strong acidic electrolyte compared to other synthesized BPC materials MM-600 and MM-800 due to higher pore volume, surface area, and optimum amount of O, N heteroatom doping.

### 3.3.2 Electrokinetic measurements

The charge-storage mechanism of BPC materials was studied by electrokinetic analysis. Pseudocapacitive properties could be observed in the BPC materials due to the presence of a redox peak in the CV diagram, as shown in Fig. 3a–c. There are two ways to store charge in pseudocapacitive electrode materials: diffusive and capacitive. Capacitive contribution is associated with the electrostatic adsorption/desorption of ions on the double layers, whereas the redox reaction provides the diffusive contribution. By analyzing the CV curves at different scan speeds according to Dunn's power law equation, we may be able to deduce how the

pseudocapacitive material stores charge. The formulas are presented in Eqs. (11) and (12) [33, 35, 36, 43, 44]:

$$i = av^b \quad (11)$$

$$\log i = \log a + b \log v \quad (12)$$

where  $a$  and  $b$  are free-floating parameters, and  $v$  represents the scan rate. The value of  $b$  can be calculated from the slope of the  $\log i$  vs.  $\log v$  graph. A value of  $0.5$  for  $a$  and  $b$  is commonly used to suggest a diffusion-controlled process, while a value of  $1$  implies a capacitive-controlled response. To determine the charge-storage mechanism of the biomass-based BPC materials synthesized in the electrokinetic experiment,  $0.5$  M  $\text{H}_2\text{SO}_4$  was utilized as a supporting electrolyte. The  $b$  values for the cathodic and anodic peaks of the BPC materials MM-600, MM-700, and MM-800 in acidic electrolytes were  $(0.72$  and  $0.54)$ ,  $(0.95$  and  $0.92)$ , and  $(0.85$  and  $0.82)$ , respectively, as shown in Fig. 3d–f. The overall charge accumulation in the active BPC electrode materials was seen by using the combined capacitive and diffusive contribution, which is illustrative of the experimental  $b$  values of the carbon nanomaterials. Capacitive contribution as a main element in the charge storage process is also recommended by the BPC framework MM-700, as shown in Fig. 3e, which has a greater value than the synthetic BPC MM-600 and MM-800. For a better understanding of the charge storage mechanism of the BPC framework, the total charge can be separated into its capacitive ( $k_1V$ ) and diffusive ( $k_2V^{1/2}$ ) components. Dunn and co-workers proposed these Eqs. (13 and 14) [33, 35, 36, 43, 44].

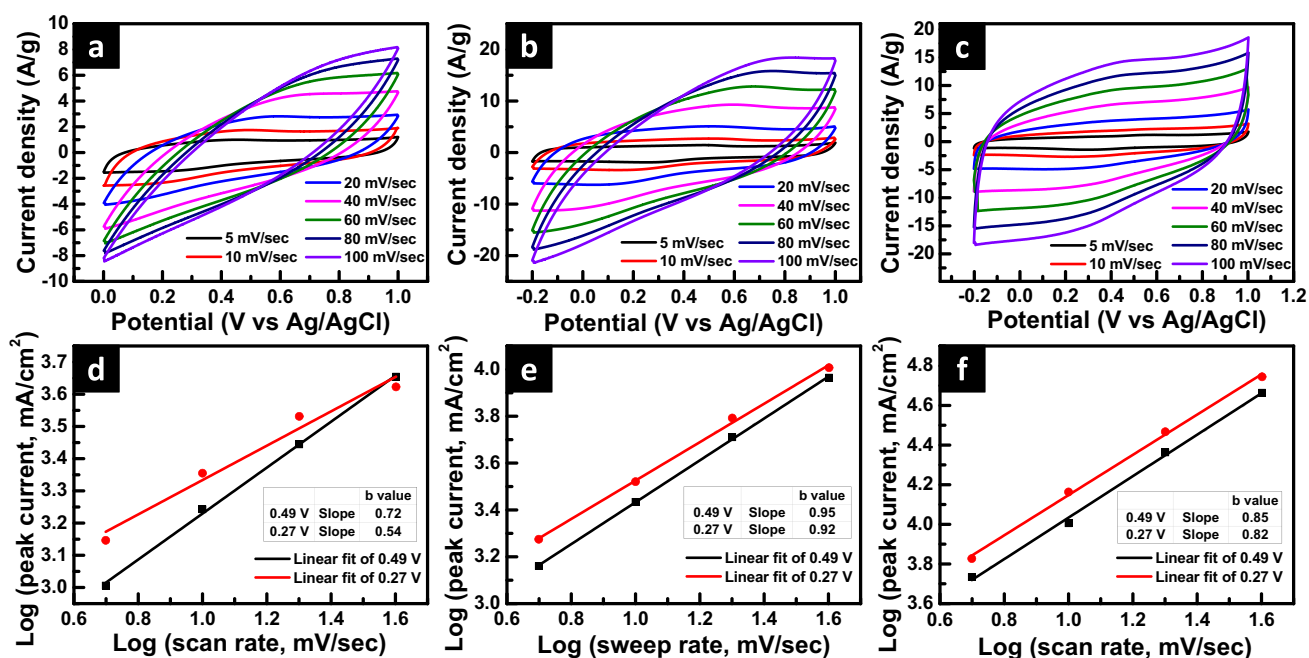


**Fig. 3** a–c Cyclic voltammograms of the synthesized BPC materials MM-600, MM-700, MM-800 at various scan rates; d–f the logarithmic plot of peak current density vs. scan rates of the synthesized BPC materials MM-600, MM-700, and MM-800



$$i(V) = k_1v + k_2v^{1/2} \tag{13}$$

$$\text{or, } \frac{i(V)}{v^{1/2}} = k_1v^{1/2} + k_2 \tag{14}$$

Using the aforementioned calculations, the capacitive contributions to the total charge amassing at a scan rate of 5 mV/s, for the synthesized BPC materials MM-600, MM-700, and MM-800, were found 41%, 85%, and 66%, respectively, as shown in Fig. 4a–c. Compared to previously produced BPC frameworks, the capacitive contribution of the MM-700 materials is the biggest towards total charge accumulation due to their larger surface area, pore volume, and heteroatoms on their carbon matrices. The contribution of capacitive and diffusive storage to the total charge storage versus different sweep rates was plotted as shown in Fig. 4d–f for the synthesized BPC materials MM-600, MM-700, and MM-800. At slow scan rates, the electrode materials’ overall charge is largely built up by the diffusion-controlled process due to the ease with which ions can be moved in the nanopores of the electroactive materials. The opposite effect occurs at very fast scan rates.

### 3.3.3 Electrochemical Impedance spectroscopic measurement

The electrochemical impedance spectroscopic measurement (EIS) was obtained between 0.1 Hz and 100 kHz to study the ion transport and charge transfer. The linear component of the Nyquist diagram at low frequencies represents the charge transfer process at the electrode/

electrolyte interface, as shown in Fig. S10, and the capacitance behavior of the electrode. The diameter of the semicircle represents the charge transfer resistance ( $R_{ct}$ ) in the high-frequency region and the equivalent series resistance ( $R_s$ ), which includes the intrinsic resistance of the electrode material, electrolyte ionic resistance, and the contact resistance between the electrolyte and electrode, is represented by the intercept on the horizontal axis [51]. As shown in Fig. S10, the BPC-based electrode MM-700 has a substantially smaller semicircle diameter and intercept than MM-600 and MM-800, indicating lower  $R_s$  and  $R_{ct}$ . Both samples exhibit nearly vertical lines in the low-frequency domain, which is indicative of perfect EDLC behavior and low impedance. The computed Nyquist diagram was generated using an equivalent electric circuit and is depicted in Fig. S10 that sheds light on the EIS behavior. When the calculated curve agrees with the measured curve (Msd), it means that the equivalent electric circuit can describe the complete behavior of the supercapacitor [52]. The synthesized BPC frameworks MM-600, MM-700, and MM-800 show respectively  $R_{ct}$  values of 6.39, 2.36, and 3.56  $\Omega$  in an acidic electrolyte. Compared to other synthesized nanomaterials, the  $R_{ct}$  of BPC framework MM-700 shows higher electron carrier efficiency at the electrode/electrolyte interface. Because of its larger surface area, larger pore volume, and BPC structure, MM-700 materials have a lower  $R_{ct}$  compared to MM-600 and MM-800. The enhanced electrochemical performance of the BPC framework MM-700 can be attributed in part to the higher efficiency with which electrons can be transferred.

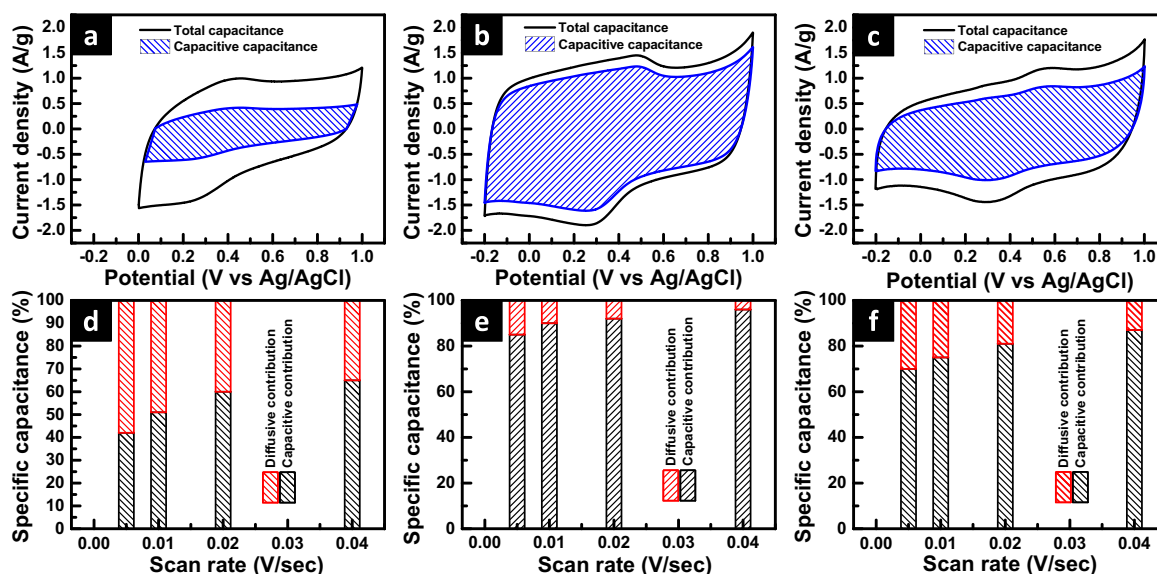


**Fig. 4** Capacitive and diffusive contribution plots of as-prepared BPC materials (a) MM-600, (b) MM-700, and (c) MM-800 materials at fixed scan rate in a three-electrode system. d, e, f Bar diagram

of the capacitive and diffusive contribution of the synthesized BPC MM-600, MM-700, and MM-800 materials at various scan rates in a three-electrode system

### 3.3.4 Real device fabrication

A solid-state symmetric device has been built to test the efficacy of the BPC material MM-700 sample using PVA- $\text{H}_2\text{SO}_4$  gel electrolyte. The electrochemical performance of the MM-700 electrode was also tested with a two-electrode setup, and the findings are shown in Fig. 5. Further supporting the carbon samples' optimal electrical double-layer capacitance behavior, the CV curves of the MM-700 electrodes in Fig. 5a showed reasonably regular rectangular forms in the two-electrode system. Note that the fabricated device's CV curve region is the largest of the three samples, suggesting that it may have the highest specific capacitance.

CV and GCD curves were recorded in the voltage range of 0 to 1.8 V to explore possible applications since the quasi-rectangular form of CV was maintained even if the voltage window stretched to 1.8 V (Fig. 6a). Figure 5a and b displays the CV curves and GCD profiles for scanning rates ranging from 10 to 100 mV/s and current densities ranging from 1 to 30 A/g, respectively. Even at a fast scan rate of 100 mV/s, all CV curves are nearly rectangular, indicative of the characteristic EDLC trait. The quasi-triangular shape of the GCD curves and the lack of a noticeable IR decrease across a range of current densities in Fig. 5b indicates low equivalent series resistance and high electrochemical reversibility. The BPC MM-700 electrode has a calculated specific capacitance of 119 F/g at 1 A/g current density, and it retains a high value of 41 F/g at 30 A/g even at the 30-fold current density. An energy storage device's energy and power densities are crucial in a commercial setting.

The highest energy density of the manufactured MM-700 is 55.55 Wh/kg at 1 A/g current density, while the maximum power density is 13.284 kW/kg at 30 A/g current density. When compared to other carbon-based supercapacitors made from biomass, such as those made from maize husk [52], rice straw [53], *Gardenia jasminoides* Ellis flowers [54], and phoenix fallen leaves [55], is significantly higher. Compared to previously reported porous carbon materials, the energy and power density achieved by devices built from synthetic porous carbon materials is higher, providing a significant advantage in practical applications. A comparative study of energy and power density of porous carbon materials is shown in Table S1.

### 3.3.5 Device stability

It is well known that supercapacitors, to be useful, must have high performance over a long number of cycles. So, in our case, we have to find the chemical stability of the synthesized BPC carbon materials.

The cycle stability of the synthesized BPC materials has been examined using three- and two-electrode systems. In a three-electrode system, the synthesized nanomaterials have 95% specific capacitance retention even after 5000 continuous charge-discharge cycles in strong acidic electrolytes. In curiosity, the stability of BPC materials in fabricated solid-state devices has been also checked. The fabricated device displays 97% specific capacitance retention even after 5000 continuous charge-discharge cycles in strong acidic electrolytes. The hierarchical porous structure, large active surface

**Fig. 5** a, b CV and CD of the fabricated solid-state device of synthesized MM-700; c comparative diagram of specific capacitance vs. scan rates; d comparative diagram of specific capacitance vs. current densities of the fabricated solid-state device

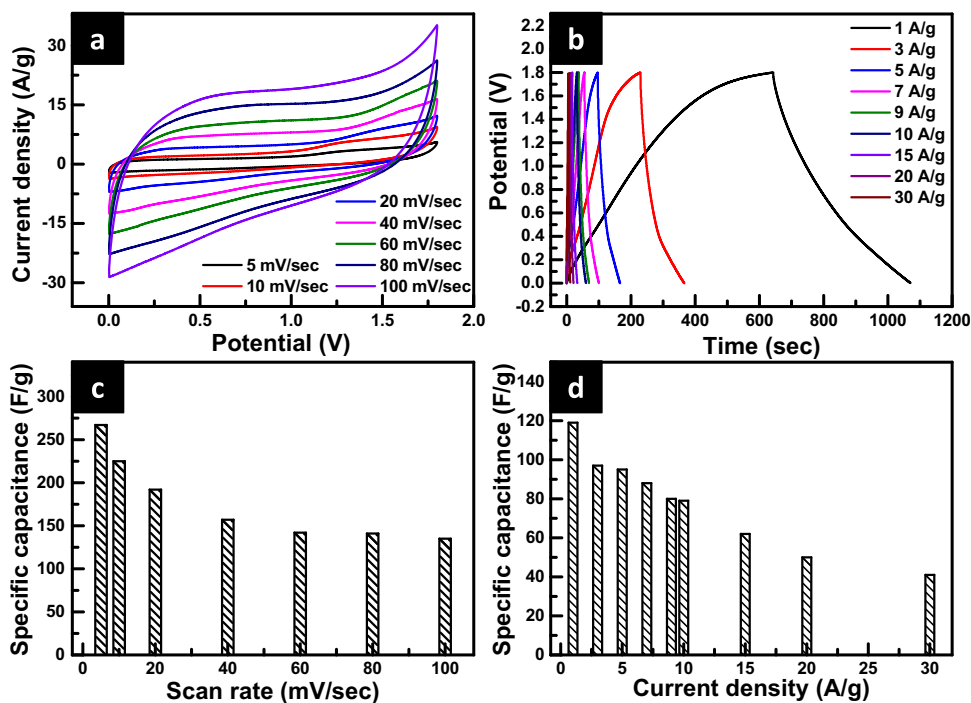
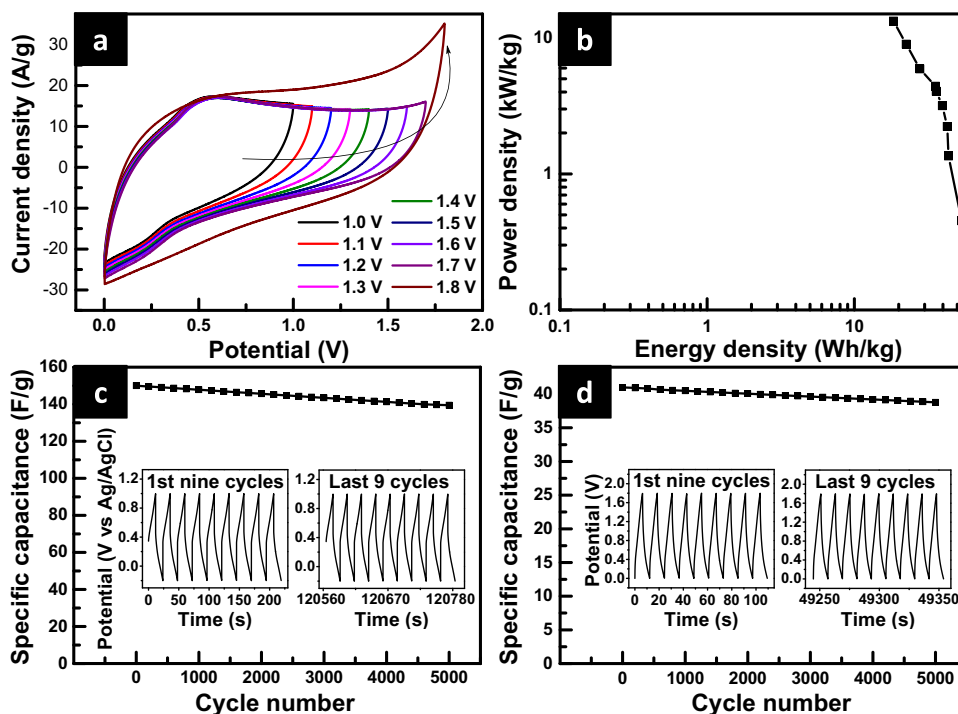


**Fig. 6** **a** Comparative CV diagrams of the fabricated solid-state device of MM-700; **b** Ragone plot of the device; **c** cyclability test of the MM-700 electrode materials in three-electrode system; **d** cyclability test of the solid-state device of MM-700. Inset: demonstration before and after CD cycles during stability test



area, and high O, N contents of the electrode material BPC MM-700 were achieved by using KOH as the pore-forming agent and melamine as the pore modifier and nitrogen supplier. More active sites and unobstructed routes for ion transfer were made possible by the hierarchical porous structure and broad surface area, while electron conductivity, wettability with electrolyte, and pseudocapacitance were all enhanced by the rich O, N-containing functional groups. High specific capacitance, excellent long cycle life, and high specific energy are just some of the results of the synergistic effect of various entry points on MM-700's capacitive performance.

## 4 Conclusions

By chemically activating biomass products with ammonium chloride and potassium hydroxide in the presence of an inert atmosphere that provides a confinement reaction medium, we present a sustainable and green synthesis approach for obtaining highly porous carbons. This method of synthesis results in carbons with a number of desirable qualities, including tuneable porosity, strong electronic conductivity, specific oxygen and nitrogen doping, and a high BET surface area and pore volume. High yields of these carbon compounds are also achieved, proving their potential for industrial scalability. Such an approach has a lot of promise for implementation because of the low cost of the precursor and the simple process. Strong capacitive energy harvesting also requires the as-prepared materials' structural advantages, such as an acceptable pore size distribution and suitable heteroatom doping. As a result, the optimized carbon nanosheet

supercapacitor composed by MM-700 provides an appealing specific capacitance of 393 F/g at the current density of 1 A/g, reasonable rate capability, and long calendar life. The fabricated solid-state device displays a higher power density of 13.284 kW/kg. Moreover, the synthesized BPC materials display excellent stability in both electrode systems using strong acidic electrolytes. Therefore, the synthesized BPC materials are promising candidate for future energy storage device electrode materials.

**Supplementary Information** The online version contains supplementary material available at <https://doi.org/10.1007/s42114-024-00833-6>.

**Author contribution** Mohammed Jalalah, HyukSu Han, Arpan Kumar Nayak, and Farid A. Harraz initiated the study, performed the extensive experiments related to the growth of the samples and preparation of devices, and wrote the paper. All authors read and approved the final manuscript.

**Funding** The authors are thankful to the Deanship of Scientific Research at Najran University for funding this work, under the Distinguished Research Program grant code (NU/DRP/SERC/12/7).

**Availability of data** The data that support the findings of this study are available from the corresponding author upon reasonable request.

## Declarations

**Conflict of interest** The authors declare no competing interests.

## References

- Guan BY, Yu L, Lou XW (2016) Formation of asymmetric bowl-like mesoporous particles via emulsion-induced interface

- anisotropic assembly. *J Am Chem Soc* 138:11306–11311. <https://doi.org/10.1021/jacs.6b06558>
2. Lin Z, Li X, Zhang H, Bin Xu B, Wasnik P, Li H, Singh MV, Ma Y, Li T, Guo Z (2023) Research progress of MXenes and layered double hydroxides for supercapacitors. *Inorg Chem Front* 10:4358–4392. <https://doi.org/10.1039/d3qi00819c>
  3. Zhang C, Shen K, Li B, Li S, Yang S (2018) Continuously 3D printed quantum dot-based electrodes for lithium storage with ultrahigh capacities. *J Mater Chem A Mater* 6:19960–19966. <https://doi.org/10.1039/c8ta08559e>
  4. Hao L, Ning J, Luo B, Wang B, Zhang Y, Tang Z, Yang J, Thomas A, Zhi L (2015) Structural evolution of 2D microporous covalent triazine-based framework toward the study of high-performance supercapacitors. *J Am Chem Soc* 137:219–225. <https://doi.org/10.1021/ja508693y>
  5. Xu H, Wu C, Wei X, Gao S (2018) Hierarchically porous carbon materials with controllable proportion of micropore area by dual-activator synthesis for high-performance supercapacitors. *J Mater Chem A Mater* 6:15340–15347. <https://doi.org/10.1039/c8ta04777d>
  6. Su H, Zhang H, Liu F, Chun F, Zhang B, Chu X, Huang H, Deng W, Gu B, Zhang H, Zheng X, Zhu M, Yang W (2017) High power supercapacitors based on hierarchically porous sheet-like nanocarbons with ionic liquid electrolytes. *Chem Eng J* 322:73–81. <https://doi.org/10.1016/j.cej.2017.04.012>
  7. Yang W, Yang W, Ding F, Sang L, Ma Z, Shao G (2017) Template-free synthesis of ultrathin porous carbon shell with excellent conductivity for high-rate supercapacitors. *Carbon NY* 111:419–427. <https://doi.org/10.1016/j.carbon.2016.10.025>
  8. Fechner N, Fellingner TP, Antonietti M (2013) “salt templating”: a simple and sustainable pathway toward highly porous functional carbons from ionic liquids. *Adv Mater* 25:75–79. <https://doi.org/10.1002/adma.201203422>
  9. Borchardt L, Oschatz M, Kaskel S (2016) Carbon materials for lithium sulfur batteries - ten critical questions. *Chem Eur J* 22:7324–7351. <https://doi.org/10.1002/chem.201600040>
  10. Gu W, Yushin G (2014) Review of nanostructured carbon materials for electrochemical capacitor applications: advantages and limitations of activated carbon, carbide-derived carbon, zeolite-templated carbon, carbon aerogels, carbon nanotubes, onion-like carbon, and graphene. *Wiley Interdiscip Rev. Energy Environ* 3:424–473. <https://doi.org/10.1002/wene.102>
  11. Kim Y, Cho CY, Kang JH, Cho YS, Moon JH (2012) Synthesis of porous carbon balls from spherical colloidal crystal templates. *Langmuir* 28:10543–10550. <https://doi.org/10.1021/la3021468>
  12. Sun L, Tian C, Li M, Meng X, Wang L, Wang R, Yin J, Fu H (2013) From coconut shell to porous graphene-like nanosheets for high-power supercapacitors. *J Mater Chem A Mater* 1:6462–6470. <https://doi.org/10.1039/c3ta10897j>
  13. Qiao Y, He J, Zhou Y, Wu S, Li X, Jiang G, Jiang G, Demir M, Ma P (2023) Flexible all-solid-state asymmetric supercapacitors based on PPy-decorated SrFeO<sub>3-δ</sub> perovskites on carbon cloth. *ACS Appl Mater Interfaces*. <https://doi.org/10.1021/acsami.3c10189>
  14. Xu RH, Ma PP, Liu GF, Qiao Y, Hu RY, Liu LY, Demir M, Jiang GH (2023) Dual-phase coexistence design and advanced electrochemical performance of Cu<sub>2</sub>MoS<sub>4</sub> electrode materials for supercapacitor application. *Energy Fuels* 37:6158–6167. <https://doi.org/10.1021/acs.energyfuels.2c04273>
  15. Hu RY, Liu LY, He JH, Zhou Y, Wu SB, Zheng MX, Demir M, Ma PP (2023) Preparation and electrochemical properties of bimetallic carbide Fe<sub>3</sub>Mo<sub>3</sub>C/Mo<sub>2</sub>C@carbon nanotubes as negative electrode material for supercapacitor. *J Energy Storage* 72:108656. <https://doi.org/10.1016/j.est.2023.108656>
  16. Liu L, Liu G, Wu S, He J, Zhou Y, Demir M, Huang R, Ruan Z, Jiang G, Ma P (2023) Fe-substituted SrCoO<sub>3</sub> perovskites as electrode materials for wide temperature-tolerant supercapacitors. *Ceram Int* 50:1970–1980. <https://doi.org/10.1016/j.ceramint.2023.10.301>
  17. Jiao Z, Chen Y, Du M, Demir M, Yan F, Zhang Y, Wang C, Gu M, Zhang X, Zou J (2023) In-situ formation of morphology-controlled cobalt vanadate on CoO urchin-like microspheres as asymmetric supercapacitor electrode. *J Alloys Compd* 958:170489. <https://doi.org/10.1016/j.jallcom.2023.170489>
  18. Yao F, Pham DT, Lee YH (2015) Carbon-based materials for lithium-ion batteries, electrochemical capacitors, and their hybrid devices. *Chemsuschem* 8:2284–2311. <https://doi.org/10.1002/cssc.201403490>
  19. Zhong Y, Liu D, Yang Q, Qu Y, Yu C, Yan K, Xie P, Qi X, Guo Z, Toktarbay Z (2023) Boosting microwave absorption performance of bio-gel derived Co/C nanocomposites. *Eng Sci* 1–12. <https://doi.org/10.30919/es988>
  20. Vijeata A, Chaudhary GR, Umar A, Chaudhary S (2021) Distinctive solvatochromic response of fluorescent carbon dots derived from different components of aegle marmelos plant. *Eng Sci* 15:197–209. <https://doi.org/10.30919/es8e512>
  21. Thota SP, Bag PP, Vadlani PV, Belliraj SK (2022) Plant biomass derived multidimensional nanostructured materials: a green alternative for energy storage. *Eng Sci* 18:31–58. <https://doi.org/10.30919/es8d664>
  22. Kang F, Jiang X, Wang Y, Ren J, Xu BB, Gao G, Huang Z, Guo Z (2023) Electron-rich biochar enhanced Z-scheme heterojunctioned bismuth tungstate/bismuth oxyiodide removing tetracycline. *Inorg Chem Front* 6045–6057. <https://doi.org/10.1039/d3qi01283b>
  23. Cai J, Xi S, Zhang C, Li X, Helal MH, El-Bahy ZM, Ibrahim MM, Zhu H, Singh MV, Wasnik P, Xu BB (2023) Overview of biomass valorization: case study of nanocarbons, biofuels and their derivatives. *J Agric Food Res* 14. <https://doi.org/10.1016/j.jafr.2023.100714>
  24. Ruan J, Chang Z, Rong H, Alomar TS, Zhu D, AlMasoud N, Liao Y, Zhao R, Zhao X, Li Y, Xu BB (2023) High-conductivity nickel shells encapsulated wood-derived porous carbon for improved electromagnetic interference shielding. *Carbon NY* 213:118208. <https://doi.org/10.1016/j.carbon.2023.118208>
  25. Guo J, Xi S, Zhang Y, Li X, Chen Z, Xie J, Zhao X, Liu Z, Colorado H, El-Bahy ZM, Abdul W (2023) Biomass based carbon materials for electromagnetic wave absorption: a mini-review. *ES Food and Agroforestry* 13:1–10. <https://doi.org/10.30919/esfaf900>
  26. Ferrero GA, Fuertes AB, Sevilla M (2015) N-porous carbon capsules with tunable porosity for high-performance supercapacitors. *J Mater Chem A Mater* 3:2914–2923. <https://doi.org/10.1039/c4ta06022a>
  27. Almeida VC, Silva R, Acerce M, Junior OP, Cazetta AL, Martins AC, Huang X, Chhowalla M, Asefa T (2014) N-doped ordered mesoporous carbons with improved charge storage capacity by tailoring N-dopant density with solvent-assisted synthesis. *J Mater Chem A Mater* 2:15181–15190. <https://doi.org/10.1039/c4ta02236j>
  28. Jalalah M, Sasmal A, Nayak AK, Harraz FA (2023) Rapid, external acid-free synthesis of Bi<sub>2</sub>WO<sub>6</sub> nanocomposite for efficient supercapacitor application. *J Taiwan Inst Chem Eng* 143:104697
  29. Jalalah M, Sivasubramaniam SS, Aljafari B, Irfan M, Almasabi SS, Alsuwian T, Khazi MI, Nayak AK, Harraz FA (2022) Biowaste assisted preparation of self-nitrogen-doped nanoflakes carbon framework for highly efficient solid-state supercapacitor application. *J Energy Storage* 54:105210
  30. Li Y, Li J, Li Y, Wang XX, Cao AC (2013) Antimicrobial constituents of the leaves of Mikania micrantha H. B. K. *PLoS One* 8. <https://doi.org/10.1371/journal.pone.0076725>
  31. Gong Y, Li D, Luo C, Fu Q, Pan C (2017) Highly porous graphitic biomass carbon as advanced electrode materials for supercapacitors. *Green Chem* 19:4132–4140. <https://doi.org/10.1039/c7gc01681f>

32. Kang X, Zhu H, Wang C, Sun K, Yin J (2018) Biomass derived hierarchically porous and heteroatom-doped carbons for supercapacitors. *J Colloid Interface Sci* 509:369–383. <https://doi.org/10.1016/j.jcis.2017.09.013>
33. Jalalah M, Rudra S, Aljafari B, Irfan M, Almasabi SS, Alsuwian T, Patil AA, Nayak AK, Harraz FA (2022) Novel porous heteroatom-doped biomass activated carbon nanoflakes for efficient solid-state symmetric supercapacitor devices. *J Taiwan Inst Chem Eng* 132:104148. <https://doi.org/10.1016/j.jtice.2021.11.015>
34. Jalalah M, Rudra S, Aljafari B, Irfan M, Almasabi SS, Alsuwian T, Patil AA, Nayak AK, Harraz FA (2022) Novel porous heteroatom-doped biomass activated carbon nanoflakes for efficient solid-state symmetric supercapacitor devices. *J Taiwan Inst Chem Eng* 132. <https://doi.org/10.1016/j.jtice.2021.11.015>
35. Rudra S, Deka N, Nayak AK, Pradhan M, Dutta GK (2022) Facile hydrothermal synthesis of Au-Mn<sub>3</sub>O<sub>4</sub> decorated graphene oxide nanocomposites for solid-state supercapacitor. *J Energy Storage* 50:104615. <https://doi.org/10.1016/j.est.2022.104615>
36. Jalalah M, Rudra S, Aljafari B, Irfan M, Almasabi SS, Alsuwian T, Khazi MI, Nayak AK, Harraz FA (2022) Sustainable synthesis of heteroatom-doped porous carbon skeleton from *Acacia auriculiformis* bark for high-performance symmetric supercapacitor device. *Electrochim Acta* 414:140205. <https://doi.org/10.1016/j.electacta.2022.140205>
37. Dastan D, Chaure N, Kartha M (2017) Surfactants assisted solvothermal derived titania nanoparticles: synthesis and simulation. *J Mater Sci Mater Electron* 28:7784–7796. <https://doi.org/10.1007/s10854-017-6474-9>
38. Zhang W, Zhu X, Liang L, Yin P, Xie P, Dastan D, Sun K, Fan R, Shi Z (2021) Significantly enhanced dielectric permittivity and low loss in epoxy composites incorporating 3d W-WO<sub>3</sub>/BaTiO<sub>3</sub> foams. *J Mater Sci* 56:4254–4265. <https://doi.org/10.1007/s10853-020-05536-z>
39. Monsef R, Ghiyasiyan-Arani M, Salavati-Niasari M (2019) Utilizing of neodymium vanadate nanoparticles as an efficient catalyst to boost the photocatalytic water purification. *J Environ Manage* 230:266–281. <https://doi.org/10.1016/j.jenvman.2018.09.080>
40. Salavati-Niasari M, Fereshteh Z, Davar F (2009) Synthesis of oleylamine capped copper nanocrystals via thermal reduction of a new precursor. *Polyhedron* 28:126–130. <https://doi.org/10.1016/j.poly.2008.09.027>
41. Asadzadeh M, Tajabadi F, Dastan D, Sangpour P, Shi Z, Taghavinia N (2021) Facile deposition of porous fluorine doped tin oxide by Dr. Blade method for capacitive applications. *Ceram Int* 47:5487–5494. <https://doi.org/10.1016/j.ceramint.2020.10.131>
42. Yang J, Zhu X, Wang H, Wang X, Hao C, Fan R, Dastan D, Shi Z (2020) Achieving excellent dielectric performance in polymer composites with ultralow filler loadings via constructing hollow-structured filler frameworks. *Compos Part A Appl Sci Manuf* 131:105814. <https://doi.org/10.1016/j.compositesa.2020.105814>
43. Arun Kumar S, Rudra S, Thamizharasan G, Pradhan M, Rani B, Sahu NK, Nayak AK (2022) Crystal structure controlled synthesis of tin oxide nanoparticles for enhanced energy storage activity under neutral electrolyte. *J Mater Sci Mater Electron* 33:13668–13683. <https://doi.org/10.1007/s10854-022-08302-w>
44. Rudra S, Thamizharasan JKG, Pradhan M, Rani B, Sahu NK, Nayak AK (2022) Fabrication of Mn<sub>3</sub>O<sub>4</sub>-WO<sub>3</sub> nanoparticles based nanocomposites symmetric supercapacitor device for enhanced energy storage performance under neutral electrolyte. *Electrochim Acta* 406:139870. <https://doi.org/10.1016/j.electacta.2022.139870>
45. Jerigová M, Odziomek M, López-Salas N (2022) “We Are Here!” oxygen functional groups in carbons for electrochemical applications. *ACS Omega* 7:11544–11554. <https://doi.org/10.1021/acsomega.2c00639>
46. Rudra S, Chakraborty R, Maji PK, Koley S, Nayak AK, Paul D, Pradhan M (2019) Intercalation pseudocapacitance in chemically stable Au- $\alpha$ -Fe<sub>2</sub>O<sub>3</sub>-Mn<sub>3</sub>O<sub>4</sub> composite nanorod: towards highly efficient solid-state symmetric supercapacitor device. *Electrochim Acta* 324:134865. <https://doi.org/10.1016/j.electacta.2019.134865>
47. Guo F, Jiang X, Jia X, Liang S, Qian L, Rao Z (2019) Synthesis of biomass carbon electrode materials by bimetallic activation for the application in supercapacitors. *J Electroanal Chem* 844:105–115. <https://doi.org/10.1016/j.jelechem.2019.05.004>
48. Song Z, Duan H, Li L, Zhu D, Cao T, Lv Y, Xiong W, Wang Z, Liu M, Gan L (2019) High-energy flexible solid-state supercapacitors based on O, N, S-tridoped carbon electrodes and a 3.5 V gel-type electrolyte. *J Chem Eng* 372:1216–1225. <https://doi.org/10.1016/j.cej.2019.05.019>
49. Chen Y, Hu R, Qi J, Sui Y, He Y, Meng Q, Wei F, Ren Y (2019) Sustainable synthesis of N/S-doped porous carbon sheets derived from waste newspaper for high-performance asymmetric supercapacitor. *Mater Res Express* 6. <https://doi.org/10.1088/2053-1591/ab2d97>
50. Gao Y, Zhang Y, Li A, Zhang L (2018) Facile synthesis of high-surface area mesoporous biochar for energy storage via in-situ template strategy. *Mater Lett* 230:183–186. <https://doi.org/10.1016/j.matlet.2018.07.106>
51. Zhou C, Zhang Y, Li Y, Liu J (2013) Cheng Zhou, Yangwei Zhang, Yuanyuan Li and Jinping Liu. *Nano Lett* 13:2078–2085
52. Usha Rani M, Nanaji K, Rao TN, Deshpande AS (2020) Corn husk derived activated carbon with enhanced electrochemical performance for high-voltage supercapacitors. *J Power Sources* 471:228387. <https://doi.org/10.1016/j.jpowsour.2020.228387>
53. Zhu L, Shen F, Smith RL, Yan L, Li L, Qi X (2017) Black liquor-derived porous carbons from rice straw for high-performance supercapacitors. *Chem Eng J* 316:770–777. <https://doi.org/10.1016/j.cej.2017.02.034>
54. Qin C, Wang S, Wang Z, Ji K, Wang S, Zeng X, Jiang X, Liu G (2021) Hierarchical porous carbon derived from *Gardenia jasminoides* Ellis flowers for high performance supercapacitor. *J Energy Storage* 33:102061. <https://doi.org/10.1016/j.est.2020.102061>
55. Zhang F, Xiao X, Gandla D, Liu Z, Tan DQ, Ein-Eli Y (2022) Bio-derived carbon with tailored hierarchical pore structures and ultra-high specific surface area for superior and advanced supercapacitors. *Nanomaterials* 12. <https://doi.org/10.3390/nano12010027>

**Publisher's Note** Springer Nature remains neutral with regard to jurisdictional claims in published maps and institutional affiliations.

Springer Nature or its licensor (e.g. a society or other partner) holds exclusive rights to this article under a publishing agreement with the author(s) or other rightsholder(s); author self-archiving of the accepted manuscript version of this article is solely governed by the terms of such publishing agreement and applicable law.